Engineered Science

RESEARCH PAPER

View Article Online

Preparation of Transparent Dispersions with Monodispersed Ag Nanoparticles for TiO_2 Photoelectrode Materials with Excellent Photovoltaic Performance

Rikui Chen,[1] Jun Bao,[1] Zhe Yan,[1] Xiejun Huang,[1] Jimmy Yun,[2] Xiaofei Zeng,[1*] and Jianfeng Chen[1,3]

Here, we demonstrate that the introduction of the monodispersed nanoparticles into photoelectrode materials can obviously improve the photovoltaic performance of dye-sensitized solar cells (DSSCs). The highly transparent dispersions of TiO_2 and Ag nanoparticles with the excellent stability were synthesized respectively. As seed crystals, monodispersed TiO_2 nanoparticles with the diameter of about 5 nm have unique advantages in regulating the growth of multi-branched TiO_2 nanowire arrays (T-MB-TiO_2), which have large specific area. Ag nanoparticles monodispersed in n-hexane with a small particle size (about 8 nm of average diameter) were incorporated into above-mentioned T-MB-TiO_2 to fabricate the T-MB-TiO_2/Ag composite photoanode, which combines the advantages of T-MB-TiO_2 with the direct electron transport channels and Ag nanoparticles with the localized surface plasmon resonance effect. Therefore, the DSSCs with the composite photoanode achieved excellent photoelectric performance, as high as the short-circuit current density (J_{sc}) of 24 mA/cm^2 and the photoelectric conversion efficiency (PCE) of 10%. Compared with the cell assembled by the photoanode of pure TiO_2 nanowire arrays grown on the FTO glass directly, J_{sc} and PCE of the cell with T-MB-TiO_2/Ag composite photoanode has been increased by 48% and 28% respectively, which has a great application potential in the fields of solar cells and photocatalysis.

Keywords: Transparent dispersion; Monodispersed nanoparticle; Multi-branched; Photoelectrode

Received 28 February 2019**, Accepted** 11 May 2019

DOI: 10.30919/es8d514

1. Introduction

Since dye-sensitized solar cells (DSSC) was reported by Grätzel's group in 1990s,[1] it has received wide attention due to its low cost, environmental friendliness, and facile fabrication process.[1-4] Typical DSSCs use TiO_2 as the photoanode, and the control of its morphology and crystalline structure has been the focus of research. Granular TiO_2, one-dimensional (1D) TiO_2 nanowires,[5,6] nanorods[7,8] and nanotubes[9-11] have been developed successively. Compared with the granular, 1D TiO_2 has a direct electron transport channel, which can rapidly transfer photogenerated electrons to the external circuit, contributing to the effective separation of electron-hole pairs.[12] However, pure 1D structures of TiO_2 are usually limited in the specific surface area, which affects their adsorption amount of the sensitizer, resulting in a decrease in the utilization of sunlight. Fortunately, preparation of TiO_2 nanowires with multiple branches or hierarchical structures is one of the effective ways to make up for this deficiency, which take advantages of the direct electron transport channel of the linear structures and the high specific surface area of the multiple branches.[13-16]

Generally, the preparation of 1D structured TiO_2 by hydrothermal or solvothermal method requires laying seed crystals on the conductive substrate. It is common in the existing reports to directly use the FTO particles on the substrate as the seeds[5,17,18] or use a sol-gel method[6,19,20] to produce granular TiO_2 seeds on the substrate. Such seed crystals are not controllable in size and the particles are usually not regular, resulting that it is difficult to regulate the growth of 1D TiO_2.

In addition to designing and controlling the morphological structure of 1D TiO_2, another important and effective way to increase the photoelectric conversion efficiency (PCE) of DSSC is adding noble metal to the 1D TiO_2 to form a composite photoanode. Noble metals such as Au, Ag can increase the light absorption of the photoanode and generate localized surface plasmon resonance (LSPR) effect,[21] resulting in transferring energy to adjacent TiO_2 or sensitizer, making electron-hole pair easier to generate and separate.[22-27] Thus, photocurrent is improved and further the PCE of DSSCs is improved. Particularly, as a noble metal with a significantly lower price, Ag has an advantage in cost. Lu[23] et al. reported the photovoltaic application of Ag/TiO_2 nanorod composites and the PCE of devices increased by 19% compared with the pure TiO_2 nanorods. In the current researches, the addition of Ag tends to be achieved by the in-situ reduction methods, such as in-situ ultraviolet light reduction[23,27,28] and chemical reduction of silver precursor.[24,29] However, these preparation processes are not easy to control the morphology and distribution of Ag nanoparticles on 1D TiO_2. If the noble metal has been synthesized in advance as a nanodispersion and then incorporated with TiO_2, the structure of composite photoanode will be easier to control and the cell may achieve better performance.

In this work, the highly transparent TiO_2 and Ag nanodispersions were synthesized and firstly employed to fabricate the 1D structured TiO_2 photoanode of DSSCs. The multi-branched anatase TiO_2 nanowires arrays (T-MB-TiO_2) were prepared by the hydrothermal method using

[1]*State Key Laboratory of Organic-Inorganic Composites, Beijing University of Chemical Technology, Beijing 100029, China*
[2]*School of Chemical Science and Engineering, The University of New South Wales Energy Physics, Sydney NSW 2052, Australia*
[3]*Research Center of the Ministry of Education for High Gravity Engineering and Technology, Beijing University of Chemical Technology, Beijing 100029, China*
****E-mail:** zengxf@mail.buct.edu.cn*

the monodispersed TiO_2 nanoparticles in transparent dispersion as seed crystals. Subsequently, the prepared Ag nanoparticles in n-hexane were incorporated into the TiO_2 nanowires arrays by spin-coating to form a T-MB-TiO_2/Ag composite photoanode. Monodispersed TiO_2 nanoparticles contribute to fabricating TiO_2 nanowire arrays with regular arrangement and dense structure. Cooperation with Ag nanoparticles can increase the visible absorption of TiO_2 nanowire arrays. With the synergistic effect of two kinds of monodispersed nanoparticles, the prepared cell with the composite photoanode gives a high PCE of 10.0%. The mechanisms of corresponding performance enhancement were also investigated.

2. Experimental

2.1 Materials and setup

Silver nitrate, 85% (v/v) hydrazine hydrate and Oleic acid were purchased from Sinopharm Chemical Reagent Co., Ltd. (shanghai, China). Hexane, anhydrous ethanol, isopropanol, toluene, sodium hydroxide, diethylene glycol (DEG) were obtained from Beijing Tongguang Fine Chemical Co., Ltd. (China). Dipotassium titanium oxide dioxalate (PTO, ≥ 98.0%) was purchased from Shanghai Dibai Chemical Technology Co., Ltd. (China). Fluorine-doped tin oxide (FTO) glasses (TEC 15, 14 Ω/square) were supplied by Nippon Sheet Glass Co., Ltd. (Japan). N719 dye was purchased from sigma-aldrich Trading Co., Ltd. (Shanghai, China). Hexachloroplatinic acid hexahydrate was obtained from Tianjin Guangfu Fine Chemical Research Institute (China). Titanium tetrachloride, acetonitrile, tert-butanol, iodine, anhydrous lithium iodide, 4-tert-butylpyridine, 1, 2-dimethyl-3-propylimidazolium iodide (DMPII) were purchased from Aladdin Reagent Co., Ltd. (Shanghai, China). All reagents were used without any further purification. The Deionized water used throughout the experiments was obtained from Smart-S30 Pure Water System (Shanghai Hitech Instruments Co., Ltd.). The core equipment for preparing nanoparticle dispersions is a rotating packed bed (RPB) which used as a reactor, and the structure and characteristics of the RPB reactor can be referred to our previous work.[30-32]

2.2 Preparation of transparent dispersions with monodispersed nanoparticles

The TiO_2 nanodispersions were prepared according to our previous report.[33] The typical preparation process of Ag nanodispersions is as follows. 744 ml of solution composed of ethanol, water, oleic acid and n-hexane (15:10:4:2 by volume) was mixed with 4.8 g of NaOH under magnetic stirring to form a mixed solution, and then 60 ml of a 0.2 mol/L aqueous solution of $AgNO_3$ was added dropwise to the above solution under continuously stirring. The stirring was continued for 30 min to form a mixture A. 85% (v/v) hydrazine hydrate ($N_2H_4 \cdot H_2O$) was formulated into 60 ml of a 7 mol/L hydrazine hydrate aqueous solution, and stirred to form a homogeneous mixture B. The mixtures A, B were pumped into RPB reactor simultaneously, and the resultant mixture was collected at the outlet. The schematic diagram is shown in Fig. 1. When the A and B were depleted, the obtained intermediate product was again introduced into the RPB through a feed tube. After 5 min of recycling, the obtained product was finally collected. The rotating speed of RPB was set to 1500 rpm throughout the reaction. The collected product was washed three times with ethanol, and the resulting precipitate was dispersed in n-hexane, followed by three times of rotary evaporation to remove ethanol. Finally, the resulting precipitate was redispersed in n-hexane to form a transparent dispersion of Ag nanoparticles.

2.3 Preparation of photoanodes

The multi-branched TiO_2 nanowire arrays were prepared via a facile template-free solvothermal method. Before the procedure of solvothermal reaction, FTO glasses were cleaned with acetone and isopropanol for several times by ultrasound. Then they were coated with a 5 wt% solid content of TiO_2 nanodispersion to form a seed crystal layer by spin coating at 2200 rpm, 30 s, followed by calcination at 500 °C for 30 min in air. Subsequently, the procedure of solvothermal is as follows. First, 0.35 g of potassium titanium oxide oxalate dehydrate (PTO) was dissolved in 15 mL of diethylene glycol (DEG) under magnetic stirring for 45 min at 40 °C. Then 5 mL deionized water was added dropwise to the mixture. After continuous stirring for 15 min, the resulting mixture was transferred to a 50 mL of Teflon-lined stainless steel autoclave, in which the FTO glass coated with a TiO_2 seed crystal layer was placed against the wall. The solvothermal reaction was carried out at 200 °C for 12 h. After the reaction system cooled to room temperature, the as-prepared TiO_2 on FTO was rinsed alternately with deionized water and ethanol, and then heated to 500 °C for 30 min in air. Then it was immersed in a 150 mM $TiCl_4$ solution for 30 min at 70 °C. After washing with water and ethanol, it was heated in air at 500 °C for 30 min again. Thus, the photoanode was obtained, denoted as T-MB-TiO_2 (multi-branched anatase TiO_2 nanowires arrays grown by using the monodispersed TiO_2

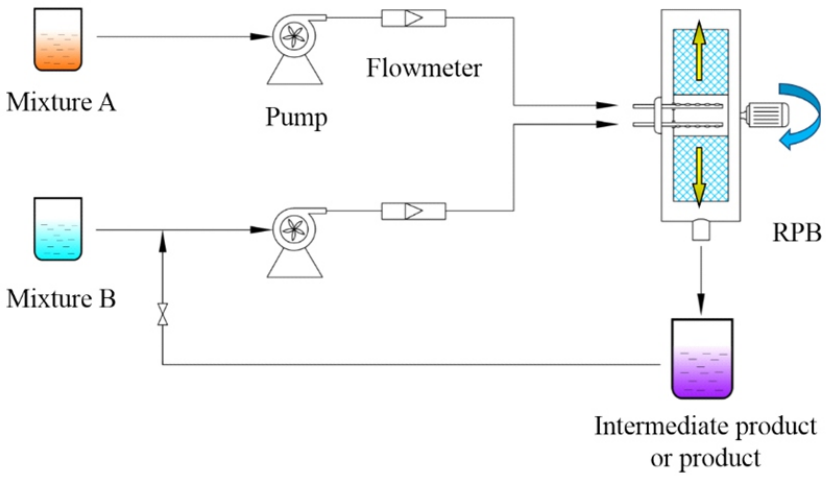

Fig. 1 Schematic diagram of the preparation process of Ag nanoparticles dispersion.

nanoparticles as seed crystals). For comparison, the photoanode of multi-branched anatase TiO_2 nanowires arrays grown by directly using FTO particles as seed crystals was prepared under the same processing conditions, denoted as F-MB-TiO_2.

The T-MB-TiO_2/Ag composite photoanode was obtained by spin-coating the transparent Ag nanodispersion on the T-MB-TiO_2 photoanode mentioned above, and then heated to 500 °C for 30 min in air to remove the organic solvents and oleic acid on the surface of Ag nanoparticles. Specially, it is worth to note that the cooling procedure of the composite photoanode needs to be carried out under the protection of Ar atmosphere to prevent the oxidation of Ag nanoparticles. A brief schematic diagram of the preparation process and the structure of T-MB-TiO_2/Ag composite photoanode are shown in Fig. 2.

2.4 Fabrication of dye sensitized solar cells

The obtained photoanodes with an active area of 0.25 cm^2 were immersed into a dye solution (0.5 mM N719 in a mixture of tert-butanol and acetonitrile solvent (1:1 by volume)) for 24 h at room temperature. Following the immersion process, the sensitized films were rinsed with acetonitrile and dried in air. For the counter electrodes, 60 µL of 5 mM H_2PtCl_6 isopropyl alcohol solution was dropped onto FTO glasses of 2 cm × 2 cm, and annealed at 400 °C for 25 min in air. The photoanode were assembled with the counter electrode using a 50 µm thick Bynel film spacer. And the liquid electrolyte (0.6 M 1,2-dimethyl-3-propylimidazolium iodide, 0.5 M tert-butylpyridine, 0.05 M lithium iodide and 0.05 M iodine) was injected into the assembled cell through small holes and then sealed by Surlyn and a cover glass.

2.5 Characterization and measurements

The morphology and structure of samples were acquired using transmission electron microscope (TEM, Hitachi HT7700, Japan) at an accelerating voltage of 100 kv, high resolution transmission electron microscope and selected area electron diffraction (HRTEM and SAED, Hitachi H-9500, Japan) at an accelerating voltage of 200 kv, atomic force microscope (AFM, Bruker, Germany) in tapping mode, and scanning electron microscopy (SEM, Hitachi S-4800, Japan) at an accelerating voltage of 5 kv. The mapping mode of Energy Dispersive Spectrometer (EDS) attached to SEM was used to examine the distribution of elements. The crystalline structure of samples was characterized by X-ray diffraction (XRD, Rigaku, Japan) equipped with Cu Kα radiation (k = 0.15418 nm) at 40 kV at a scanning rate of 5°/min. The dynamic light scattering (DLS) with zetasizer (Marlvern Zetasizer Nano ZS90, UK) was used to test the size of particle in the dispersion. UV-Vis spectrophotometer (Shimadzu, UV-2600, Japan) was used to measure the absorbance of samples. And the Diffuse reflectance spectra (DRS) measurements were performed by UV-Vis-NIR spectrometer (PerkinElmer Lambda 950, USA) with an integrating sphere. X-ray photoelectron spectroscopy (XPS, SHIMADZU AXIS SUPRA, Japan) was used to analyze the composition, contents and their chemical valence states of the elements in samples. Ultraviolet photoelectron spectroscopy (UPS, SHIMADZU AXIS SUPRA, Japan) equipped with He I light source (21.22 eV) was used to determine the work function of photoanode materials. Inductively coupled plasma-Optical Emission Spectrometer (ICP-OES, Thermo Scientific ICAP 6300 radial, England) was used to determine the content of each element in samples. The sheet resistance of the photoanode materials was tested by a four-probe tester (RTS-8, Guangzhou, China). Current density-voltage (J-V) plots was measured using Keithley model 2420 digital source meter under a standard light intensity of 100mW/cm^2 from Air Mass (AM) 1.5 solar simulator. Incident photon-to electron conversion efficiency (IPCE) were tested with monochromatic light from a 300 W xenon lamp and a monochromator (Newport 2936-R,

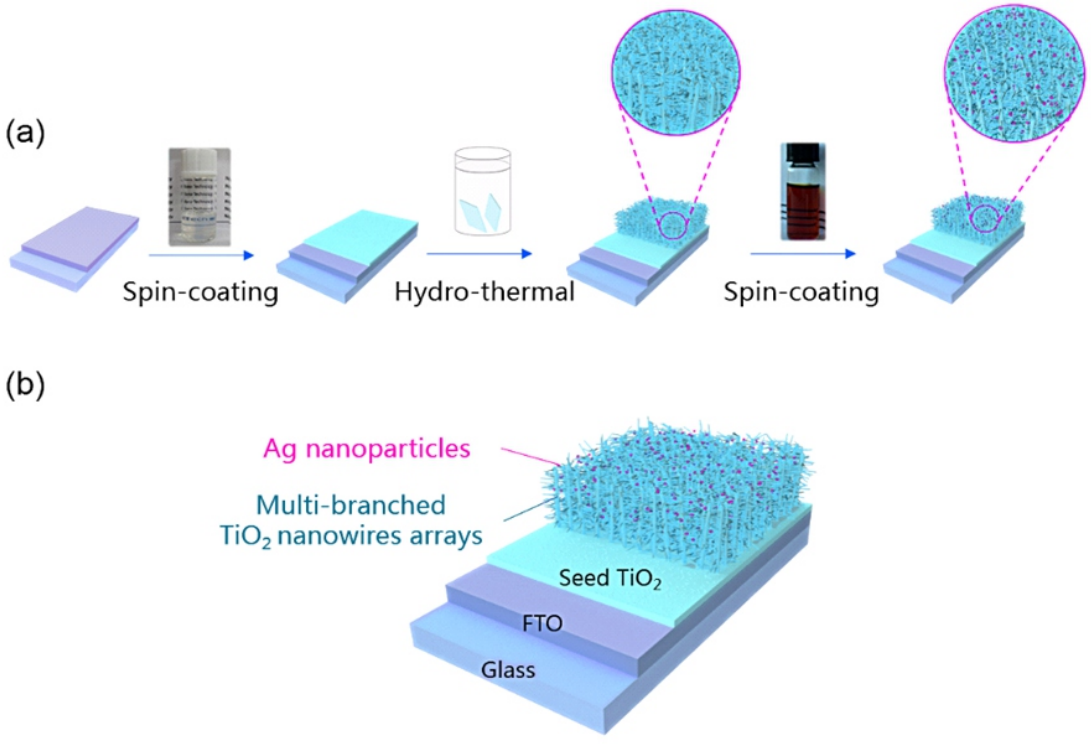

Fig. 2 Schematic diagram of (a) the preparation process of T-MB-TiO_2/Ag composite photoanode, (b) the structure of T-MB-TiO_2/Ag composite photoanode.

USA) and the measurement system is calibrated with a standard silicon cell. Electrochemical impedance spectroscopy (EIS) was performed using an electrochemical workstation (CHI660E, Shanghai, China) with a test frequency range of 0.1 Hz - 10^5 Hz, an initial potential of open-circuit potential, and an amplitude of 10 mV.

3. Results and discussion

3.1 Characterization of the TiO_2 and Ag nanodispersions

Herein, the prepared TiO_2 nanoparticles have an average particle diameter of 5 nm and a narrow particle size distribution, which are monodispersed in toluene to form a transparent nanodispersion with excellent stability. More detailed morphology and properties of TiO_2 nanoparticles could refer to our previous report.[33] The morphology and structure of monodispersed Ag nanoparticles were characterized and the results are shown in Fig. 3. From the digital photo of the dispersion (Fig. 3a), it can be seen that the dispersion exhibits a brownish red appearance with the high transparency, indicating that the nanoparticles are well-dispersed in the dispersion. The TEM image was shown in Fig. 3b, Ag nanoparticles exhibit a spheroidal shape with a small particle size of about 8nm. The arrangement of particles is very regular and there is a certain spacing among each particle, which demonstrated that nanoparticles display a monodispersed state in n-hexane. From the HRTEM image of Ag nanoparticles (Fig. 3c), the lattice fringes can be clearly observed. The spacing between the lattice fringes is 0.236 nm, which corresponds to the (111) crystallographic facet of the face-centered cubic (*fcc)* silver.[34] The SAED pattern (inset of Fig. 3c) shows that Ag nanoparticles are polycrystalline structures, and their diffraction rings appear at the positions corresponding to the (111), (200), (220), (311) and (331) crystallographic facets[31] respectively, as indicated by the red arrows in the inset. To further confirm the particle size distribution and dispersibility of Ag nanoparticles, dynamic light scattering test was performed and the results are shown in Fig. 3d. The average particle size of Ag nanoparticles is about 8 nm, which is consistent with the particle size observed in TEM. The range of particle size distribution is very narrow. It also reveals that the Ag nanoparticles are very well-dispersed. The Fig. 3e depicts the UV-Vis absorption spectrum of the Ag nanodispersion. The strong absorption peak at 409 nm demonstrates that Ag nanoparticles can absorb part of visible light contributing to the

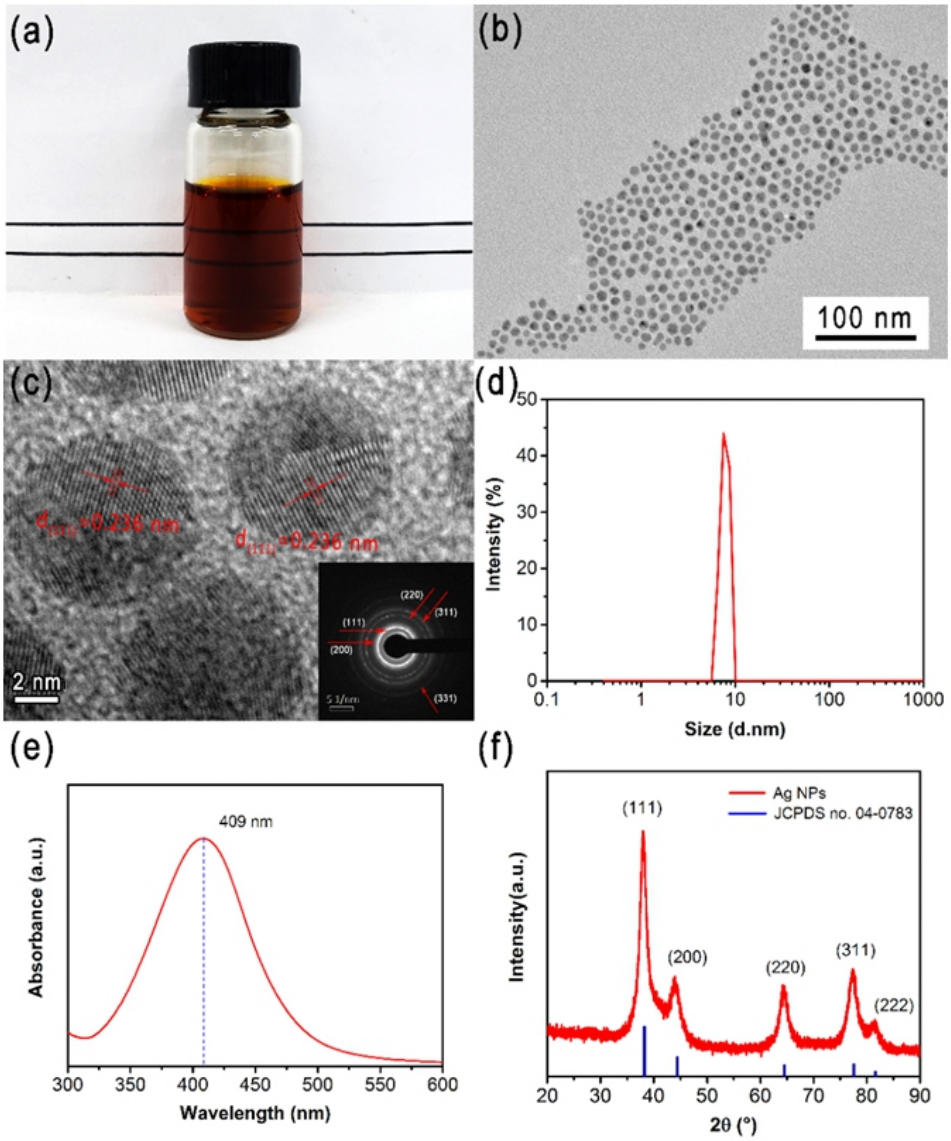

Fig. 3 (a) Digital photograph, (b) TEM image, (c) HRTEM and SAED (inset) images, (d) particle size distribution, (e) UV-Vis spectrum and (f) XRD spectrum of Ag nanodispersions.

absorption and utilization of light by the composite photoanodes. The phase structure of the as-prepared Ag nanoparticles was characterized by XRD shown in Fig. 3f. The diffraction peaks at around 38.0°, 44.0°, 64.4°, 77.4° and 81.5° can be assigned to (111), (200), (220), (311) and (222) crystallographic facets of *fcc* silver (JCPDS no. 04-0783), respectively.[35]

3.2 Characterization of the T-MB-TiO_2/Ag composite photoanodes

The surface of FTO coated with TiO_2 seeds was characterized by AFM, and the results are shown in Fig. 4. It can be seen that the surface of FTO coated with TiO_2 seeds is flat and the roughness is about 12 nm after TiO_2 seeds coating. It is precisely because of the small particle size and good dispersibility of the TiO_2 nanoparticles in the transparent dispersion. Moreover, the denseness and thickness of the layer of TiO_2 seeds are controllable by adjusting the solid content of TiO_2 in the nanodispersions, which is beneficial to the fabrication of the denser and more regular TiO_2 nanowires arrays for DSCCs with the excellent properties.

Fig. 5 depicts the morphology, structure and elemental distribution of the T-MB-TiO_2/Ag composite photoanode. The SEM images of the composite photoanode are shown in Fig. 5(a, b). From the top view (Fig. 5a), it is like a lot of nano-trees arranged in an orderly way to form a nano-forest. As shown in the Fig. 5a inset, it's clear that TiO_2 manifests a multi-branched tree structure, and the nanowires penetrate each other to form a dense network structure. From the cross-section view (Fig. 5b), it shows that the thickness of the composite photoanode is approximately 22 μm. In addition, in the longitudinal direction, the photoanode shows a looser upper region and a relatively dense structure at the lower region. Since the Ag nanoparticles are not easy to distinguish with the T-MB-TiO_2 by SEM, the corresponding TEM and HRTEM images are acquired and shown in Fig. 5(c, d). It can be seen that Ag nanoparticles attached on the TiO_2 nanowires arrays, as marked in red circle in Fig. 5c. The lattice spacing of 0.352 nm and 0.236 nm can be attributed to the (101) lattice facets of anatase TiO_2 and the (111) lattice facets of Ag nanoparticles, respectively.[34,36] The sizes of Ag nanoparticles are consistent with their original sizes in the dispersion, indicating that the particle size is almost constant after annealing treatment. To further investigate the distribution of Ag nanoparticles on T-MB-TiO_2, EDS mapping measurements were carried out for T-MB-TiO_2/Ag composite photoanode and the results are shown in Fig. 5(e-g). Clearly, the elements of Ti, O and Ag are homogeneously distributed throughout the T-MB-TiO_2/Ag composite photoanode. And the homogeneous spatial distribution of Ag on the T-MB-TiO_2 might be attributed to the controllable incorporation of TiO_2 with Ag nanoparticles monodispersed in liquid medium.

The element composition and chemical state of photoanode

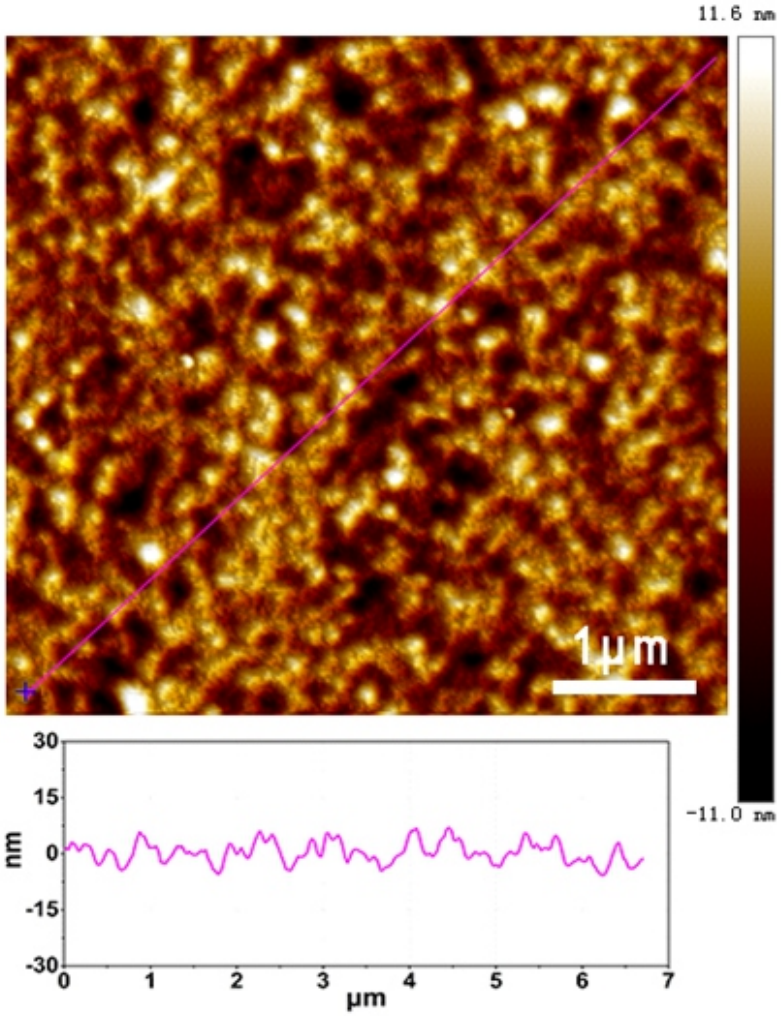

Fig. 4 AFM images of surface morphology and roughness of seed TiO_2 coated FTO.

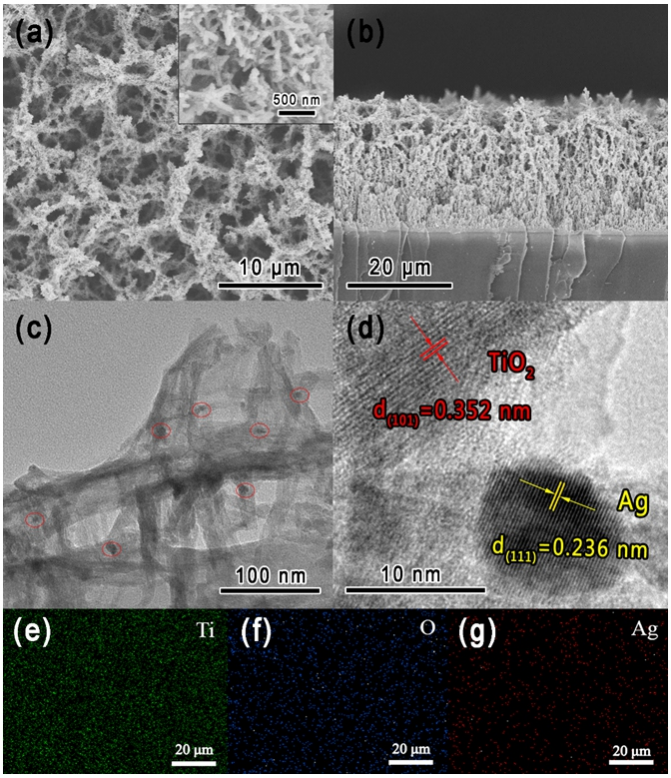

Fig. 5 T-MB-TiO_2/Ag composite photoanode, (a) SEM images of Top view at low and high magnifications (inset), (b) SEM images of Cross-section view, (c) TEM images, (d) HRTEM images, (e-g) EDS mapping images of Ti, O and Ag elements, respectively.

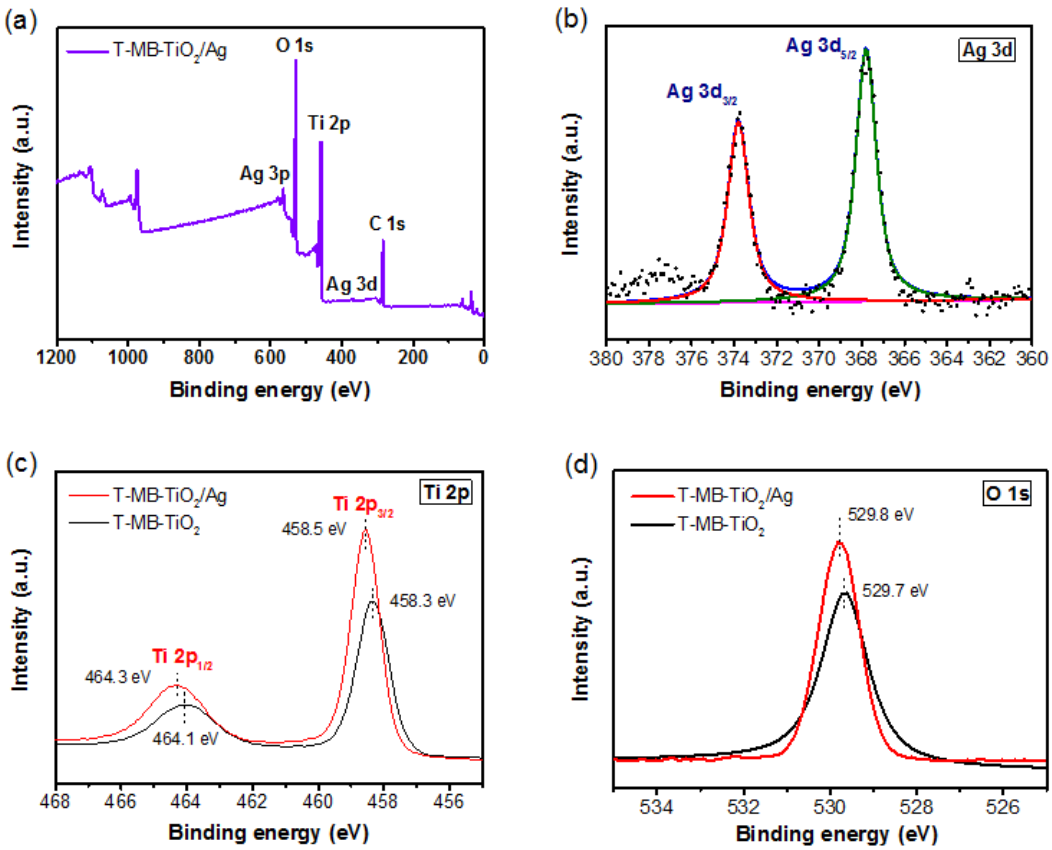

Fig. 6 XPS spectra of T-MB-TiO_2 or T-MB-TiO_2/Ag composite photoanode: (a) full range spectrum, high-resolution spectra of (b) Ag 3d, (c) Ti 2p and (d) O 1s.

materials were determined by XPS, and the results are shown in Fig. 6. The full range spectrum of T-MB-TiO_2/Ag composite (Fig. 6a) indicates the existence of Ti, O, and Ag. Further, Fig. 6b shows the high resolved XPS spectrum of Ag 3d in the T-MB-TiO_2/Ag composite. The peaks located at binding energy of 373.8 and 367.8 eV are assigned to metallic Ag $3d_{3/2}$ and Ag $3d_{5/2}$ respectively, indicating that the Ag species exist as metallic Ag^0 in T-MB-TiO_2/Ag composite photoanode without any oxidation. Compared with pure bulk metallic Ag (374.3 and 368.2 eV for Ag $3d_{3/2}$ and Ag $3d_{5/2}$, respectively),[37] the binding energy of Ag 3d has a negative shift of about 0.5 eV in the composite photoanode. Moreover, in Fig. 6(c, d), the high resolved XPS spectra of Ti 2p and O 1s were acquired both in the T-MB-TiO_2 and T-MB-TiO_2/Ag composite. As can be seen, compared with the Ti 2p in the T-MB-TiO_2, the binding energy of Ti 2p slightly increases in the T-MB-TiO_2/Ag composite (from 464.1 eV to 464.3 eV of Ti $2p_{1/2}$ and 458.3 eV to 458.5 eV of Ti $2p_{3/2}$).[38] And the similar result appears again in O 1s (from 529.7 eV to 529.8 eV).[39] Such shift of binding energy probably results from metal-support interactions between Ag nanoparticles and TiO_2 and the similar phenomenon has also been observed in Au or Ag decorated TiO_2 or ZnO systems reported in the literatures.[40-43] In addition, from the XPS results, the content of silver nanoparticles was proved to be about 1 wt% in the T-MB-TiO_2/Ag composite, which is consistent with ICP test results.

T-MB-TiO_2/Ag composite photoanode was further characterized by XRD, and the results are shown in Fig. 7. The T-MB-TiO_2 of the composite photoanode shows a highly crystalline anatase structure, and the diffraction peak position has an exact match with the standard card (JCPDS no. 21-1272).[44] Among the rutile, anatase and brookite of TiO_2, anatase TiO_2 has a higher bandgap (3.2 eV) than that of rutile TiO_2 (3.0 eV) which is beneficial for a higher open-circuit voltage of DSSCs at the same short current density. And anatase TiO_2 has a higher conduction band edge energy and lower recombination rate of electron-

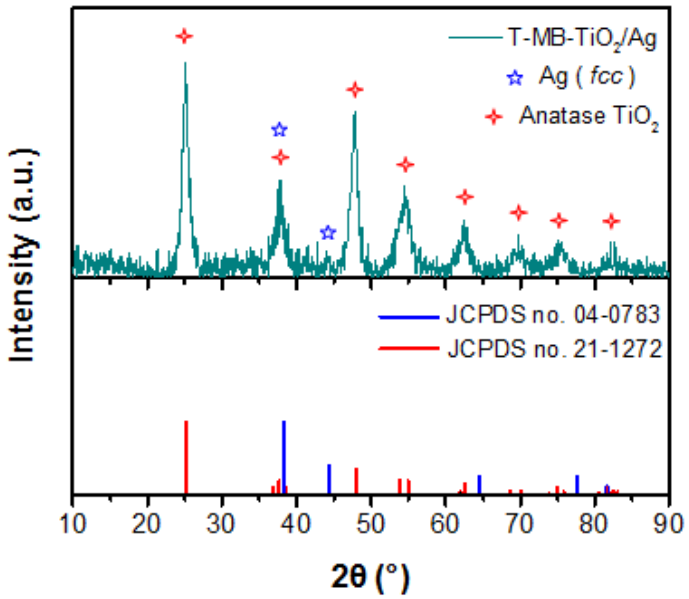

Fig. 7 XRD spectrum of T-MB-TiO_2/Ag composite photoanode.

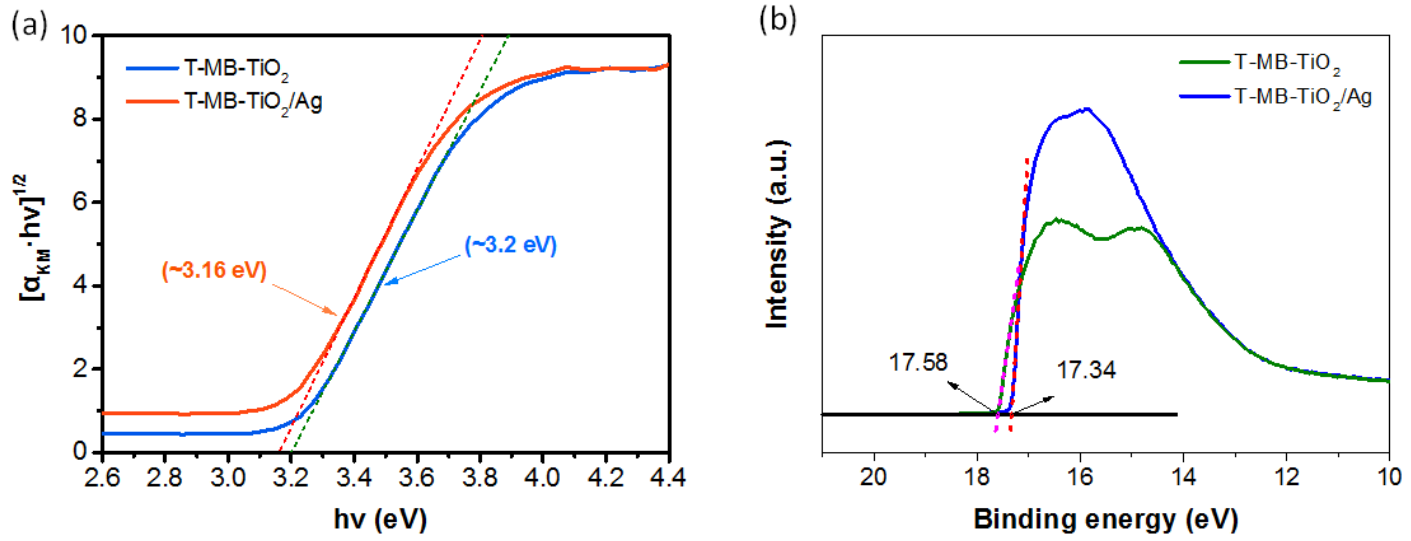

Fig. 8 (a) Tauc plots and (b) UPS spectra of T-MB-TiO_2 and T-MB-TiO_2/Ag composites.

hole pairs.[45,46] Therefore, anatase TiO_2 has been preferred. By the way, because of the small content of silver (only 1 wt%), there is no obvious diffraction peak of Ag in the XRD spectrum of the composite photoanode.[52]

3.3 Performance of solar cells

For solar cells, PCE is the most concerned performance. The J-V plots of DSSCs with F-MB-TiO_2, T-MB-TiO_2 and T-MB-TiO_2/Ag composite photoanodes were measured and the results are shown in Fig. 9. The corresponding photovoltaic parameters and dye loading amount are calculated according to the J-V plots and summarized in Table 1. As can be seen, the cell with T-MB-TiO_2/Ag composite photoanode has the highest short-circuit current density (J_{sc}), so it also achieves the highest PCE (10.0%). Compared with the cell of F-MB-TiO_2 photoanode, it has been increased by 28% in PCE. The huge improvement of PCE comes from the increase in J_{sc}, and it could be attributed to two aspects. Firstly, Ag nanoparticles have a strong LSPR effect. When the light is incident on them, the nanoparticles will strongly absorb photon energy, and the plasmon-excited hot electrons in Ag nanoparticles can be transmitted to the adjacent TiO_2 conduction band and then transmitted to the external circuit.[22] In addition, the LSPR effect induces to the strong electric field near the Ag nanoparticles, and therefore the electrons of nearby dye molecules are excited more effectively.[53,54] In short, the existence of the LSPR effect enhances the light absorption of the photoanode, which is an important reason for the high J_{sc} of DSSCs with the composite photoanode. Secondly, due to the introduction of monodispersed TiO_2 nanoparticles as the seed crystals, a dense and uniform T-MB-TiO_2 photoanode is formed, which has a larger specific surface area and more dye loading amount than the F-MB-TiO_2 photoanode. As can be seen in Table 1, the dye loading amount increases from 106.1 nmol/cm^2 of F-MB-TiO_2 to 128.8 nmol/cm^2 of T-MB-TiO_2. As a result, compared with the F-MB-TiO_2, T-MB-TiO_2 photoanode cell has a higher J_{sc}, so as well as the higher value of PCE. In summary, the enhancement of photovoltaic performance benefited from the addition of the monodispersed TiO_2 nanoparticles and Ag nanoparticles in the preparation process.

EIS measurements were used to test the charge transfer resistance of the DSSCs, and the obtained Nyquist plots are shown in Fig. 10a. Typically, the Nyquist plot for DSSCs consists of two distinct semicircles. The first semicircle is located in the high frequency region (Fig. 10a inset) and the diameter of semicircle reflects the charge transfer resistance within the FTO/Pt/electrolyte interface (R_1). The diameter of the second semicircle in the low frequency region reflects the charge transfer resistance within the photoanode/dye/electrolyte interface (R_2).[22,55,56] The resistance between the FTO substrate and TiO_2 (R_s) is reflected by the intercept of the curve on the horizontal axis. The

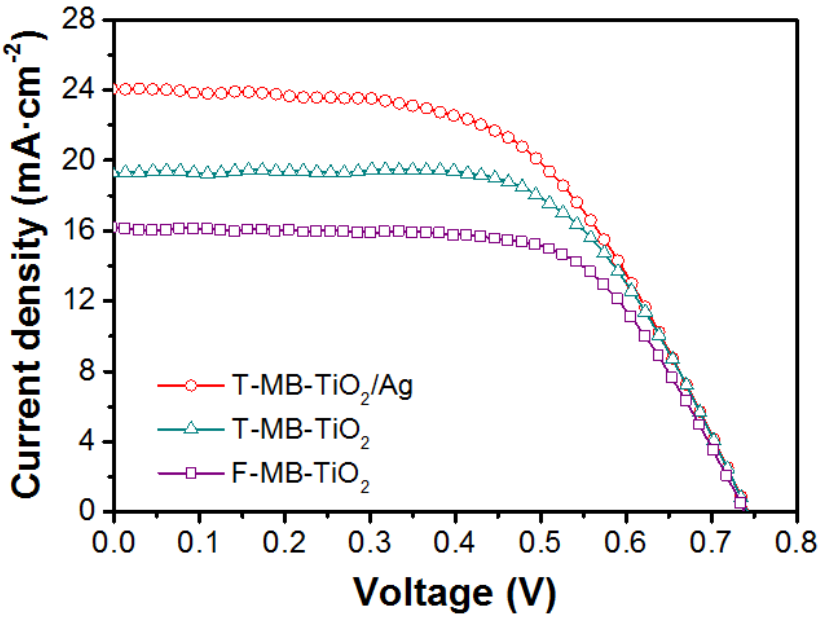

Fig. 9 J-V plots of DSSCs with F-MB-TiO_2, T-MB-TiO_2 and T-MB-TiO_2/Ag composite photoanodes.

Table 1 The dye loading amount and photovoltaic parameters of DSSCs with different photoanodes.

Photoano de	*Dye loading amount* (nmol/cm^2)	V_{oc} (V)	J_{sc} (mA/cm^2)	*FF* /	*PCE* (%)
T-MB-TiO_2/Ag composite	125.5	0.743	24.01	0.560	10.0
T-MB-TiO_2	128.8	0.744	19.36	0.631	9.1
F-MB-TiO_2	106.1	0.740	16.19	0.651	7.8

corresponding resistance values shown in Table 2 are obtained by the calculation according to the plot in Fig. 10a and the equivalent circuit in Fig. 10b. Since the conducting substrates, FTO/Pt counter electrode and the I^-/I^{3-} electrolyte used in DSSCs with F-MB-TiO_2, T-MB-TiO_2 and T-MB-TiO_2/Ag composite photoanodes are almost identical, the values of R_s and R_1 are very close. The difference lies in the transfer resistance R_2 of the photoanode/dye/electrolyte interface, which has a large impact on the performance of DSSCs. As can be seen, among the three cells composed of F-MB-TiO_2, T-MB-TiO_2 and T-MB-TiO_2/Ag composite photoanodes, the last one has the lowest value in R_2, and the next is the cell with T-MB-TiO_2 photoanode. This indicates that the charge transfer resistance within the photoanode/dye/electrolyte interfaces is greatly reduced by the addition of Ag nanoparticles, which is more advantageous for the transmission of photogenerated electrons to the negative electrode of the cells, reducing the recombination probability of photogenerated electrons and holes,[16,22,57] and thus the J_{sc} of DSSCs is improved. In addition, the sheet resistance of the T-MB-TiO_2 photoanode film is about 85 kΩ/square, and with the addition of Ag, the sheet resistance of the T-MB-TiO_2/Ag photoanode film is reduced to about 67 kΩ/square. The macroscopic conductivity of photoanode is also enhanced.

In order to further understand the reasons for the improved PCE, the DSSCs were subjected to UV-Vis absorbance and IPCE testing, and the results are shown in Fig. 11. As shown in Fig. 11a, the cell composed of the T-MB-TiO_2/Ag composite photoanode has the highest light absorption intensity in the visible range. Compared with T-MB-TiO_2 photoanode cell, the absorption intensity at 520 nm of the T-MB-TiO_2/Ag composite photoanode cell was increased by 9%, demonstrating the enhancement of light absorption by Ag NPs because of the LSPR effect. Moreover, the visible light absorption intensity of the F-MB-TiO_2 photoanode is the weakest due to the low amount of dye adsorption. Similarly, the cell assembled from T-MB-TiO_2/Ag composite photoanode has the highest IPCE values in the light wavelength range of 300-800 nm. The IPCE values of the cell composed of the T-MB-TiO_2 photoanode are higher than that of the cell composed of the F-MB-TiO_2 photoanode. A higher IPCE value verifies a higher photocurrent density,[58] which well corroborates the J-V measurement results. Furthermore, the calculated J_{sc} values by the convolution of IPCE are 19.63 mA/cm^2, 17.53 mA/cm^2 and 15.57 mA/cm^2 for the cells with T-MB-TiO_2/Ag, T-MB-TiO_2 and F-MB-TiO_2 photoanodes, respectively. The variation trend of the calculated J_{sc} from IPCE is completely consistent with that of J_{sc} obtained from the J-V results. This also reveals that the addition of TiO_2 nanoparticles and Ag nanoparticles can significantly improve the performance of DSSCs. The slight difference of calculated J_{sc} from the J-V results is probably due to the slight spectral mismatch, as reported in literature.[59-62]

Table 3 gives the comparison of photovoltaic performance of DSSCs with different 1D TiO_2 photoanodes reported in the literatures[16,23,63-69] and in this work. Obviously, the DSSC prepared in this work is more excellent in photovoltaic performance. It has the highest value of short-circuit current density among the cells in Table 3, resulting in the highest PCE value of 10.0%. A preliminary analysis of the reasons for this achievement is as follows. On the one hand, by employing monodispersed TiO_2 nanoparticles as the seed crystals, we

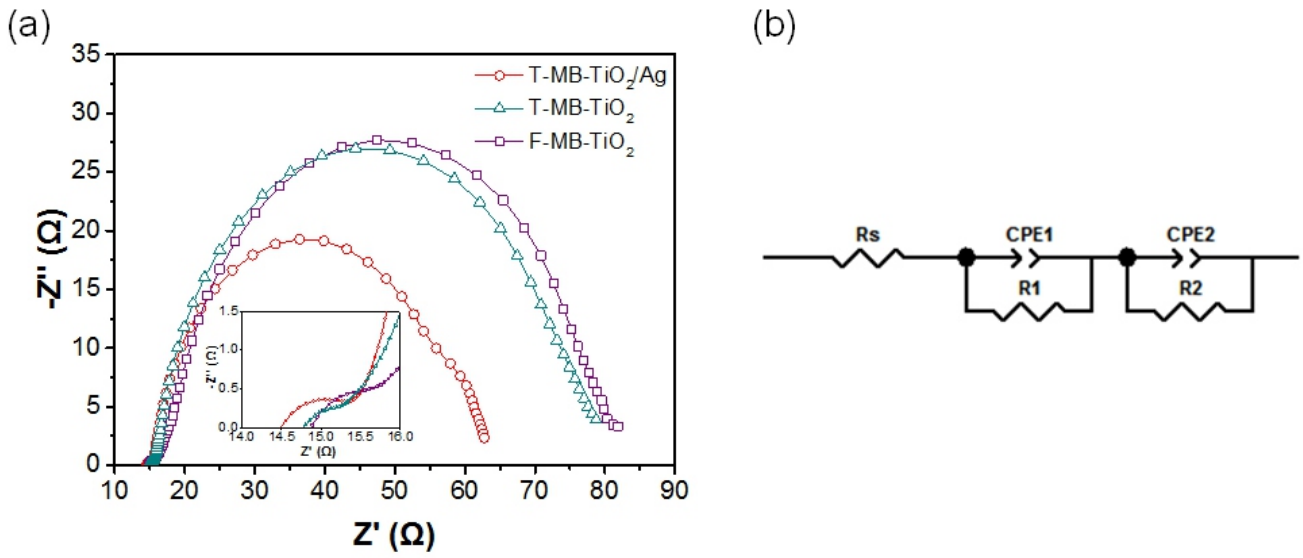

Fig. 10 (a) Nyquist plots of DSSCs with F-MB-TiO_2, T-MB-TiO_2 and T-MB-TiO_2/Ag composite photoanodes and part of plots in magnified (inset), (b) equivalent circuit of DSSCs.

Table 2 The EIS parameters of DSSCs with F-MB-TiO_2, T-MB-TiO_2 and T-MB-TiO_2/Ag composite photoanodes.

Photoanode	R_s (Ω)	R_1 (Ω)	R_2 (Ω)
T-MB-TiO_2/Ag composite	14.5	1.0	46.1
T-MB-TiO_2	14.8	1.0	61.4
F-MB-TiO_2	14.9	1.2	65.4

prepared the T-MB-TiO_2 with the high specific surface area which is sufficient to adsorb more dye molecules. As a fast transmission channel of photogenerated electrons, T-MB-TiO_2 improves the transmission efficiency and effectively reduces the recombination probability of electron-hole pairs. On the other hand, the Ag nanoparticles were prepared in advance, which ensures the advantages of nanoparticles, such as a small particle size, a narrow particle size distribution, a good crystal crystallinity and dispersibility, and then incorporated with T-MB-TiO_2. The method for preparing Ag nanoparticles into a dispersion can make Ag distribute on the T-MB-TiO_2 framework uniformly and exert its LSPR effect role more efficiently, which is a crucial point in the process.

4. Conclusions

The monodispersed TiO_2 nanoparticles with the average particle diameter of about 5 nm and monodispersed Ag nanoparticles of about 8 nm were successfully synthesized, respectively. They were all dispersed with a narrow particle size distribution and excellent stability in the liquid media. The TiO_2 nanoparticles were employed as the seed crystals to prepare T-MB-TiO_2 with the multi-branched nano-trees interlaced to each other, which has a dense and uniform morphology and the thickness is about 22 μm. Because of relatively high specific surface area, T-MB-TiO_2 photoanode can absorb more amount of dye and the DSSC assembled with it has a high PCE value of 9.1%, which is 17% higher than that of DSSC with F-MB-TiO_2 photoanode (7.8%).

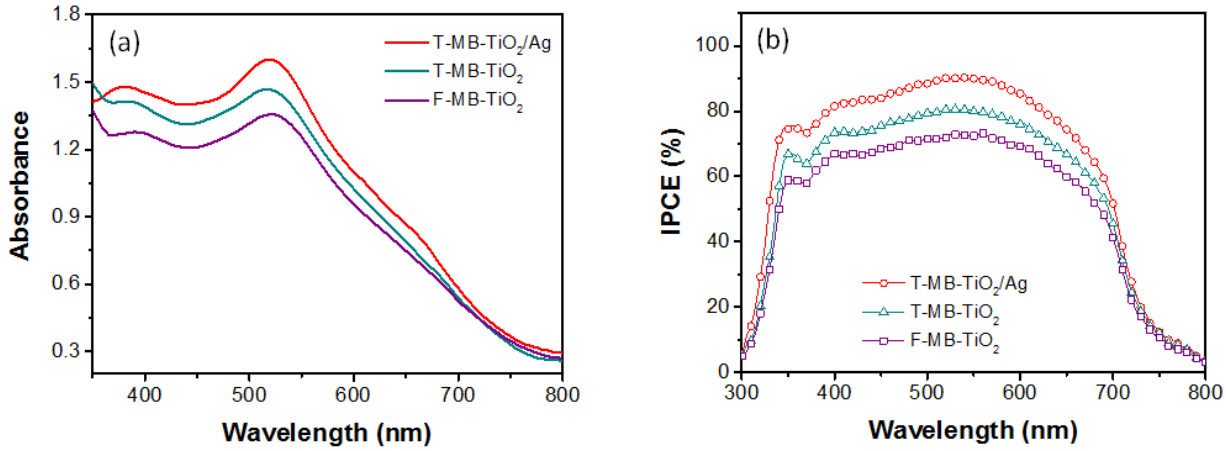

Fig. 11 (a) UV-Vis absorbance spectra, (b) IPCE plots of DSSCs with F-MB-TiO_2, T-MB-TiO_2 and T-MB-TiO_2/Ag composite photoanodes.

Table 3 Comparison of photovoltaic performance of DSSCs with photoanodes based on 1D structured TiO_2 or 1D structured TiO_2/noble metal composite.

Photoanode	V_{oc}(V)	J_{sc}(mA/cm^2)	*FF*	*PCE*(%)	*Reference*
Anatase multi -branched TiO_2 nanowires arrays/Ag nanoparticles composite	0.743	24.01	0.560	10.0	This work
Hierarchical anatase pine tree -like TiO_2	0.740	17.70	0.620	8.0	16
Anatase TiO_2 nanorods/Ag nanoparticles composite	0.710	16.46	0.592	6.9	23
Au NPs/TiO_2 nanotubes photonic crystal	0.710	11.71	0.679	5.6	63
Au NPs/TiO_2 nanotubes	0.714	14.72	0.660	6.9	64
Ag NWs/TiO_2 nanofibres	0.727	19.80	0.676	9.7	65
Ultra -long multi -layered anatase TiO_2 nanowir e arrays	0.787	18.25	0.650	9.4	66
Ultra -long rutile TiO_2 nanowire arrays	0.687	17.38	0.747	8.9	67
Porous rutile TiO_2 nanorod arrays	0.710	20.49	0.545	7.9	68
TiO_2 nanowires network coupling with Au NPs	0.790	17.38	0.710	9.73	69

Furthermore, in order to further improve the PCE of the cell, the as-prepared Ag nanoparticles were incorporated with T-MB-TiO_2 to form the T-MB-TiO_2/Ag composite photoanode. With the synergistic effect of monodispersed TiO_2 and Ag nanoparticles, the DSSC has the excellent photoelectric performance. The short-circuit current density enhanced obviously from 16.19 to 24.01 mA/cm^2, contributing to the increase in the PCE by 28%. Importantly, the advantages of uniformity and small particle size of monodispersed nanoparticles are the important prerequisite for the excellent photoelectric properties of the DSSCs.

Acknowledgments

This work was financially supported by the National Natural Science Foundation of China (21776016), the National Key Research and Development Program of China (2016YFA0201701/2016YFA0201700).

References

1. B. O'Regan and M. Grätzel, *Nature*, 1991, **353**, 737-740.
2. M. Grätzel, *Nature*, 2001, **414**, 338-344.
3. U. Bach, D. Lupo, P. Comte, J. E. Moser, F. Weissörtel, J. Salbeck, H. Spreitzer and M. Grätzel, *Nature*, 1998, **395**, 583-585.
4. C. V. Jagtap, V. S. Kadam, S. R. Jadkar and H. M. Pathan, *ES Energy Environ.*, 2018, **3**, 60-67.
5. X. J. Feng, K. Shankar, O. K. Varghese, M. Paulose, T. J. Latempa and C. A. Grimes, *Nano Lett.*, 2008, **8**, 3781-3786.
6. X. J. Feng, K. Zhu, A. J. Frank, C. A. Grimes and T. E. Mallouk, *Angew. Chem.*, 2012, **124**, 2781-2784.
7. K. Fan, W. Zhang, T. Y. Peng, J. N. Chen and F. Yang, *J. Phys. Chem. C*, 2011, **115**, 17213-17219.
8. M. K. Wang, J. Bai, F. Le Formal, S. J. Moon, L. Cevey-Ha, R. Humphry-Baker, C. Grätzel, S. M. Zakeeruddin and M. Grätzel, *J. Phys. Chem. C*, 2012, **116**, 3266-3273.
9. H. P. Jen, M. H. Lin, L. L. Li, H. P. Wu, W. K. Huang, P. J. Cheng and E. W. G. Diau, *ACS Appl. Mater. Inter.*, 2013, **5**, 10098-10104.
10. L. L. Li, Y. J. Chen, H. P. Wu, N. S. Wang and E. W. G. Diau, *Energy Environ. Sci.*, 2011, **4**, 3420-3425.
11. S. Lee, I. J. Park, D. H. Kim, W. M. Seong, D. W. Kim, G. S. Han, J. Y. Kim, H. S. Jung and K. S. Hong, *Energy Environ. Sci.*, 2012, **5**, 7989-7995.
12. P. Panneerselvam, V. Murugadoss, V. Elayappan, N. Lu, Z. H. Guo and S. Angaiah, *ES Energy Environ.*, 2018, **1**, 99-105.
13. M. D. Ye, D. J. Zheng, M. Q. Lv, C. Chen, C. J. Lin and Z. Q. Lin, *Adv. Mater.*, 2013, **25**, 3039-3044.
14. J. Y. Liao, B. X. Lei, H. Y. Chen, D. B. Kuang and C. Y. Su, *Energy Environ. Sci.*, 2012, **5**, 5750-5757.
15. L. Passoni, F. Ghods, P. Docampo, A. Abrusci, J. Martí-Rujas, M. Ghidelli, G. Divitini, C. Ducati, M. Binda, S. Guarnera, A. Li Bassi, C. S. Casari, H. J. Snaith, A. Petrozza and F. Di Fonzo, *ACS Nano*, 2013, **7**, 10023-10031.
16. D. K. Roh, W. S. Chi, H. Jeon, S. J. Kim and J. H. Kim, *Adv. Funct. Mater.*, 2014, **24**, 379-386.
17. B. Liu and E. S. Aydil, *J. Am. Chem. Soc.*, 2009, **131**, 3985-3990.
18. Z. J. Zhou, J. Q. Fan, X. Wang, W. H. Zhou, Z. L. Du and S. X. Wu, *ACS Appl. Mater. Inter.*, 2011, **3**, 4349-4353.
19. A. Kumar, A. R. Madaria and C. W. Zhou, *J. Phys. Chem. C*, 2010, **114**, 7787-7792.
20. J. J. Qiu, F. W. Zhuge, X. M. Li, X. D. Gao, X. Y. Gan, L. Li, B. B. Weng, Z. S. Shi and Y. H. Hwang, *J. Mater. Chem.*, 2012, **22**, 3549-3554.
21. M. Rycenga, C. M. Cobley, J. Zeng, W. Y. Li, C. H. Moran, Q. Zhang, D. Qin and Y. N. Xia, *Chem. Rev.*, 2011, **111**, 3669-3712.
22. Y. Y. Li, J. G. Wang, X. R. Liu, C. Shen, K. Y. Xie and B. Q. Wei, *ACS Appl. Mater. Inter.*, 2017, **9**, 31691-31698.
23. Q. P. Lu, Z. D. Lu, Y. Z. Lu, L. F. Lv, Y. Ning, H. X. Yu, Y. B. Hou and Y. D. Yin, *Nano Lett.*, 2013, **13**, 5698-5702.
24. J. Yun, S. H. Hwang and J. Jang, *ACS Appl. Mater. Inter.*, 2015, **7**, 2055-2063.
25. S. Sreeja and V. Shetty K, *Sol. Energy*, 2017, **157**, 236-243.
26. D. Zhang, W. C. H. Choy, F. X. Xie, W. E. I. Sha, X. C. Li, B. F. Ding, K. Zhang, F. Huang and Y. Cao, *Adv. Funct. Mater.*, 2013, **23**, 4255-4261.
27. G. Kawamura, H. Ohmi, W. K. Tan, Z. Lockman, H. Muto and A. Matsuda, *Nanoscale Res. Lett.*, 2015, **10**, 219-224.
28. Y. Liang, S. H. Wang and P. F. Guo, *Russ. J. Phys. Chem. A*, 2015, **89**, 2137-2141.
29. L. G. Qin, D. Y. Liu, Y. Q. Zhang, P. L. Zhao, L. S. Zhou, Y. Y. Liu, F. M. Liu and G. Y. Lu, *Electrochim. Acta*, 2018, **263**, 426-432.
30. J. F. Chen, Y. H. Wang, F. Guo, X. M. Wang and C. Zheng, *Ind. Eng. Chem. Res.*, 2000, **39**, 948-954.
31. X. W. Han, X. F. Zeng, J. Zhang, H. F. Huan, J. X. Wang, N. R. Foster and J. F. Chen, *Chem. Eng. J.*, 2016, **296**, 182-190.
32. X. J. Huang, X. F. Zeng, J. X. Wang and J. F. Chen, *Ind. Eng. Chem. Res.*, 2018, **57**, 4253-4260.
33. M. Guang, Y. Xia, D. Wang, X. F. Zeng, J. X. Wang and J. F. Chen, *Mater. Chem. Phys.*, 2019, **224**, 100-106.
34. S. K. Li, Y. H. Shen, A. J. Xie, X. R. Yu, L. G. Qiu, L. Zhang and Q. F. Zhang, *Green Chem.*, 2007, **9**, 852-858.
35. X. Z. Lin, X. W. Teng and H. Yang, *Langmuir*, 2003, **19**, 10081-10085.
36. Z. C. Lai, F. Peng, Y. Wang, H. J. Wang, H. Yu, P. R. Liu and H. J. Zhao, *J. Mater. Chem.*, 2012, **22**, 23906-23912.
37. Z. N. Yu, M. M. Xu, Q. Wang, X. W. Sun and J. Lan, *Mater. Res. Bull.*, 2018, **104**, 149-154.
38. J. Men, Q. Gao, S. Sun, X. Zhang, L. Duan and W. Lü, *Mater. Res. Bull.*, 2017, **85**, 209-215.
39. Z. B. Dong, D. Y. Ding, T. Li and C. Q. Ning, *Appl. Surf. Sci.*, 2018, **436**, 125-133.
40. R. Si, J. Liu, Y. Zhang, X. Chen, W. Dai and X. Fu, *Appl. Surf. Sci.*, 2016, **387**, 1062-1071.
41. N. P. Herring, K. AbouZeid, M. B. Mohamed, J. Pinsk and M. S. El-Shall, *Langmuir*, 2011, **27**, 15146-15154.
42. T. H. Yang, L. D. Huang, Y. W. Harn, C. C. Lin, J. K. Chang, C. I. Wu and J. M. Wu, *Small*, 2013, **9**, 3169-3182.
43. Y. Wang, H. B. Fang, Y. Z. Zheng, R. Q. Ye, T. Xia and J. F. Chen, *Nanoscale*, 2015, **7**, 19118-19128.
44. M. H. Jung, M. J. Chu and M. G. Kang, *Chem. Commun.*, 2012, **48**, 5016-5018.
45. Y. Bai, I. Mora-Seró, F. D. Angelis, J. Bisquert and P. Wang, *Chem. Rev.*, 2014, **114**, 10095-10130.
46. M. A. Waghmare, N. I. Beedri, A. U. Ubale and H. M. Pathan, *Eng. Sci.*, 2018, **6**, 36-43.
47. D. R. Coronado, G. R. Gattorno, M. E. E. Pesqueira, C. Cab, R. d. Coss and G. Oskam, *Nanotechnology*, 2008, **19**, 145605.
48. J. K. Kim, S. U. Chai, Y. Cho, L. L. Cai, S. J. Kim, S. Park, J. H. Park and X. L. Zheng, *Small*, 2017, **13**, 1702260.
49. A. Pandikumar, S. Manonmani and R. Ramaraj, *Catal. Sci. Technol.*, 2012, **2**, 345-353.
50. S. P. Lim, Y. S. Lim, A. Pandikumar, H. N. Lim, Y. H. Ng, R. Ramaraj, D. C. S. Bien, O. K. Abou-Zied and N. M. Huang, *Phys. Chem. Chem. Phys.*, 2017, **19**, 1395-1407.
51. S. P. Lim, A. Pandikumar, N. M. Huang and H. N. Lim, *RSC Adv.*, 2014, **4**, 38111-38118.
52. C. Peng, P. Wei, X. Y. Li, Y. P. Liu, Y. H. Cao, H. J. Wang, H. Yu, F. Peng, L. Y. Zhang, B. S. Zhang and K. L. Lv, *Nano Energy*, 2018, **53**, 97-107.
53. N. Chander, A. F. Khan, E. Thouti, S. K. Sardana, P. S. Chandrasekhar, V. Dutta and V. K. Komarala, *Sol. Energy*, 2014, **109**, 11-23.
54. H. L. Ran, J. J. Fan, X. L. Zhang, J. Mao and G. S. Shao, *Appl. Surf. Sci.*, 2018, **430**, 415-423.
55. J. T. Park, D. K. Roh, R. Patel, E. Kim, D. Y. Ryu and J. H. Kim, *J. Mater. Chem.*, 2010, **20**, 8521-8530.
56. M. D. Ye, C. Chen, M. Q. Lv, D. J. Zheng, W. X. Guo and C. J. Lin, *Nanoscale*, 2013, **5**, 6577-6583.
57. T. T. Xu, D. C. Kong, Z. Z. Xi, T. Huang, X. L. Qin, H. J. Wu, K. C. Kou, R. M. Wang, L. X. Chen and T. L. Ma, *Eng. Sci.*, 2019, **7**, http://dx.doi.org/10.30919/es8d698.
58. Z. Q. Li, L. E. Mo, W. C. Chen, X. Q. Shi, N. Wang, L. H. Hu, T. Hayat, A. Alsaedi and S. Y. Dai, *ACS Appl. Mater. Inter.*, 2017, **9**, 32026-32033.
59. Liu Yeru, Jennings James R., Parameswaran Manoj and W. Qing, *Energy Environ. Sci.*, 2011, **4**, 564-571.

60. W. S. Shin, J.-C. Lee, J.-R. Kim, H. Y. Lee, S. K. Lee, S. C. Yoon and S.-J. Moon, *J. Mater. Chem.*, 2011, **21**, 960-967.
61. C. J. Lin, W. Y. Yu and S. H. Chien, *J. Mater. Chem.*, 2010, **20**, 1073-1077.
62. C. J. Lin, S. J. Liao, L. C. Kao and S. Y. Liou, *J. Hazard. Mater.,* 2015, **291**, 9-17.
63. M. Guo, J. Chen, J. Zhang, H. J. Su, L. Liu, N. Q. Fu and K. Y. Xie, *Electrochim. Acta*, 2018, **263**, 373-381.
64. Z. Wang, Y. W. Tang, M. Y. Li, Y. D. Zhu, M. Y. Li, L. H. Bai, M. D. Luoshan, W. Lei and X. Z. Zhao, *J. Alloy. Compd.*, 2017, **714**, 89-95.
65. M. G. C. M. Kumari, C. S. Perera, B. S. Dassanayake, M. A. K. L. Dissanayake and G. K. R. Senadeera, *Electrochim. Acta*, 2019, **298**, 330-338.
66. W. Q. Wu, Y. F. Xu, C. Y. Su and D. B. Kuang, *Energy Environ. Sci.*, 2014, **7**, 644-649.
67. H. L. Li, Q. J. Yu, Y. W. Huang, C. L. Yu, R. Z. Li, J. Z. Wang, F. Y. Guo, S. J. Jiao, S. Y. Gao, Y. Zhang, X. T. Zhang, P. Wang and L. C. Zhao, *ACS Appl. Mater. Inter.*, 2016, **8**, 13384-13391.
68. M. Q. Lv, D. J. Zheng, M. D. Ye, J. Xiao, W. X. Guo, Y. K. Lai, L. Sun, C. J. Lin and J. Zuo, *Energy Environ. Sci.*, 2013, **6**, 1615-1622.
69. Y. C. Yen, P. H. Chen, J. Z. Chen, J. A. Chen and K. J. Lin, *ACS Appl. Mater. Inter.*, 2015, **7**, 1892-1898.